Performance evaluation of different types of building partitions in decentralized heating areas based on dynamic simulation

Qiong Chen, Nan Li & Ketong Li

Published online: 27 Jul 2021.

Submit your article to this journal

Article views: 14

View related articles

View Crossmark data

Taylor & Francis
Taylor & Francis Group

Check for updates

Performance evaluation of different types of building partitions in decentralized heating areas based on dynamic simulation

Qiong Chen, Nan Li, and Ketong Li

National Centre for International Research of Low-carbon and Green Buildings, Ministry of Science & Technology, Chongqing University, Chongqing, China

ABSTRACT

The harsh indoor environment in winter in the hot-summer and cold-winter zones of China and the increasing demand for winter heating from residential consumers have prompted more and more researchers to address the energy-efficient heating problem in non-centralized heating areas. A computational fluid dynamics model of a typical building was developed to analyze the dynamic heat transfer characteristics and energy consumption of interior partitions under decentralized heating in this region, of which the accuracy of the established model was proved by the relative error of less than 5% compared with the experimental measurement. Then seven typical kinds of interior partition configurations with different wall thickness, wall material, and insulation layer locations were developed and evaluated through simulation analysis. Transient heat storage ratio and cumulative heat storage ratio were proposed to demonstrate the dynamic heat transfer characteristics of interior partitions. The simulation results showed that 180 mm and 220 mm solid clay bricks can reduce energy consumption by 17.56% and 30.23%, respectively, compared with 120 mm solid clay bricks. The energy consumption of fly ash aerated concrete and solid clay brick partitions were reduced by 10.18% and 19.02%, respectively, compared with porous concrete partitions. The dynamic heat transfer characteristics of internal partitions with internal insulation were similar to those with external insulation due to the reduction in unnecessary energy consumption transferred to adjacent unheated rooms by about 20% compared to that without insulation. And the heat consumption of interior partitions under convective heating was 17.3% higher than under radiant heating.

1. Introduction

The low ambient winter temperatures between 0°C and 10°C in the hot-summer and cold-winter zones in China result in extremely harsh indoor thermal environments in buildings without heating systems (Sheng, Wen,L, and Zhang 2021). Unlike the centralized heating commonly used in the northern region, most residential buildings in the southern region operate intermittently with the decentralized heating operation. Previous studies illustrated that zone air temperatures are below 10°C during 78% of the heating period in winter in hot-summer and cold-winter zones with the average zone air temperature of 8.5°C, which is only about 2°C higher than the ambient air temperature, demonstrating that the indoor thermal environment of buildings in hot-summer and cold-winter zones is a serious and prompt problem during the long winter months (Wang et al. 2021; Zhang and Zhang 2020).

Residential buildings with intermittent heating for a long time are exposed to great risks of surrounding by unheated rooms where the zone air temperature is only 2°C higher than the ambient temperature, then the energy consumption transferred to the adjacent unheated rooms through the interior partitions can reach about 70% of the total heating energy consumption of the building heating system at most which should not be underestimated. In the building envelope design

and the operation management of the air conditioning system, the profound influence of the dynamic heat transfer process through the interior partitions on the indoor thermal environment and energy consumption should be comprehensively considered (Aguilar, Solano, and Vicente 2014; Natephra, Yabuki, and Fukuda 2018), especially in decentralized heating areas. It is essential to optimize the building envelope structures including geometry configurations, materials, and insulation for lower energy consumption of HVAC systems (Chorowski, Rogala, and Pyrka 2016), which can also provide a reference and guidance for design standards of thermal property parameters for building internal envelope in hot-summer and cold-winter zones.

Ozel and Pihtili conducted a study to find the optimal insulation materials and distribution of insulation in Elazığ in Turkey (Ozel and Pihtili 2007). After studying 12 kinds of wall configurations consisting of different masonry and insulation materials, with lag time and reduction factor as evaluation indicators, they found that the best thermal performance can be achieved by placing the three insulation materials on the external, middle, and internal sides, respectively, in different insulation configurations. This finding was also closely related to the area climate covered in the study. Meral Ozel studied how the daylight absorption rate and insulation affected the

CONTACT Nan Li ✉ nanlicqu@163.com 🏛 National Centre for International Research of Low-carbon and Green Buildings, Ministry of Science & Technology, Chongqing University, Chongqing 400044, China

heat transfer performance of exterior walls (Ozel 2012) and investigated the energy-saving potential of the façade. It was concluded that the daylight absorption rate of the façade had a significant effect on the annual transmission rate of both uninsulated and insulated walls though it had little effect on the average annual lag time. Following this research, Meral Ozel developed a method for determining the optimal insulation thickness of walls in hot climates based on cooling transfer loads (Ozel 2013). Simulations using the implicit finite difference method were applied and it was concluded that a north-facing wall with an insulation thickness of 3.1 cm could achieve the best economic performance during the cooling period.

Ioannis Axaopoulos et al. implemented a study on thickness, insulation material, and orientation of the façade for energy-saving and economic efficiency (Axaopoulos et al. 2015). They found that the energy savings of north-facing façades were significant and the best economic feedback can be achieved in the shortest possible time with north-facing façades. Sami A. Al-Sanea addressed the problem of the optimal R-value of building walls in different climatic regions of the Kingdom of Saudi Arabia (Al-Sanea et al. 2016). Annual heat loads were calculated of building envelopes with different insulation thicknesses to obtain the optimal R-values, while the optimal R-value ranged from 2.00 m$^2 \cdot$ K/W to 2.90 m$^2 \cdot$ K/W for Riyadh and Jeddah and ranged from 1.34 m$^2 \cdot$ K/W to 1.99 m$^2 \cdot$ K/W for Abha. The payback period for the optimum insulation thickness (L_{opt}) was found to be between 3 years and 10 years taking into account the effects of inflation and discount rate.

Dragan Cvetkovic and Milorad Boji´c aimed to optimize the thermal insulation of building envelopes equipped with radiant heating systems (Cvetković and Bojić 2014). Four radiant heating systems were studied including a floor heating system, a wall heating system, a ceiling heating system, and a newly developed floor heating system in a net-zero energy house in Kragjevac, Serbia. The experimental results showed that radiant walls required the maximum insulation thickness while the radiant floors required the minimum insulation thickness. The house with the optimal insulation thickness saved a lot of energy compared to that with conventional insulation thickness. Besides, many authors have conducted experimental and numerical researches on the insulation thickness (Cvetković and Bojić 2014; Daouas 2011; Idris and Mae 2017), the surface absorptive properties of external walls (Al-Sanea, Zedan, and Al-Hussain 2013), and the windows (Hee et al. 2015; Ihara, Gustavsen, and Jelle 2015). Chan (2012), Danielle E.M. Bond (Bond, Clark, and Kimber 2013), Mohannad Bayoumi (Bayoumi 2017), Yusuf Başoğul (Başoğul, Demircan, and Keçebaş 2016), Jérôme Barrau (Barrau, Ibañez, and Badia 2014), et al. have investigated the thermal performance of windows for different regions, different climatic conditions, and heating methods to obtain the best energy efficiency and improved indoor thermal environment (Azmi and Ibrahim 2020).

Rosti, Omidvar, and Monghasemi (2020) used life cycle cost analysis (LCCA) to optimize the insulation thickness of exterior walls for energy savings and payback period determination for exterior walls in all climate zones of Iran. Jie et al. (2019) developed an optimization model for determining the optimal economic insulation thickness of building envelopes for existing buildings with combined heat and power (CHP)-based district heating (DH) systems. Al-Tamimi et al. (2020) proposed a finite element model (FEM) to find out the optimum geometry of cavities and their layout in masonry concrete blocks for minimizing the demand for air-conditioning systems in buildings. .Huang et al. (2020) studied the new aerogel super-insulation material for thermal insulation application for energy conservation. Kumar et al. (2020) compared the property performance of different building insulation materials (thermal, hygroscopic, acoustic, reaction to fire, environmental, and cost) in different climate zones. Ziapour, Rahimi, and Gendeshmin (2020) presented a new kind of composite prefabricated wall block and further determined its optimum insulation thickness in Ardabil. In a study by La Rosa et al. (2014) a thermal conductivity analysis and an environmental analysis of various materials used in the building envelopes using the life cycle assessment (LCA) method. Özel et al. (2015) compare the transmission losses of using rock wool and glass wool as insulation materials to determine the optimum envelope insulation thickness. Amiri Rad and Fallahi (2019) carried out a comprehensive analysis of the materials and optimal insulation thickness of the facades of office buildings based on energy, environmental, and economic criteria.

In general, previous studies have focused on the heat transfer performance and energy consumption of the building envelopes (Chang, Castro-Lacouture, and Yamagata 2020; Mathur and Damle 2021), including the construction, materials, window-to-wall ratios, and insulation layer locations of exterior walls (Hu et al. 2019; Li, Zhang, and Li 2021). However, the influence of dynamic heat transfer performance of the internal partitions on energy consumption and indoor thermal environment should be also emphasized in hot-summer and cold-winter areas of China with dominating decentralized heating (Yamamoto et al. 2021). The thermal property parameters of the interior partitions are rarely given enough attention while that of the external envelopes are specified in the relevant building design standards. The lack of scientific standards for the design of internal partitions can lead to a significant reduction in the energy efficiency of the heating system (Xu et al. 2020). In decentralized heating areas, there is still a gap in the research on the influence of the internal building envelope on the indoor thermal environment and energy consumption. Most of the current research on the heat transfer characteristics of building envelopes focuses on steady-state heat transfer processes (Al-Sanea and Zedan 2011; Asdrubali et al. 2014), while the scientific research on the dynamic heat transfer characteristics of the internal envelope is still lacking.

In this research, a computational fluid dynamics (CFD) model of a typical building is developed to study the dynamic heat transfer characteristics of interior partitions in hot-summer and cold-winter zones in China, and an experimental platform is built to verify the accuracy of the established CFD model by comparing the experimental results with the

simulation results. The influence factors such as the partition thickness, material, location of the insulation layer, and heating method on dynamic heat transfer characteristics of internal partitions and energy consumption of the heating system are evaluated through numerical simulation. The research results can provide some reference and guidance for optimizing the internal building envelopes in hot-summer and cold-winter zones and improving the energy efficiency of decentralized heating systems.

Nomenclature	
a	Thermal diffusion coefficient of interior partitions, m^2/s.
l	Half the thickness of the inner wall, m.
λ	Thermal conductivity coefficient of interior partitions, $W/m \cdot K$.
a	Convective heat transfer coefficient of interior partitions, $W/m^2 \cdot K$.
$t_b(\tau)$	Zone air temperature, $^\circ C$.

2. Dynamic heat transfer process of interior partition

The step-change of the heat supply of the building thermal zones during the intermittent operation of the heating or cooling system creates a step internal disturbance effect for the transient heat transfer process of the building envelopes. The building envelopes experience the process of heat storage and heat releases under step internal disturbance, of which the dynamic performance depends on specific parameters such as the envelope configuration, material property, and location and thermal property of insulation layers. Therefore, it is essentially important to explore and analyze the dynamic heat transfer performance of building envelopes under the step internal disturbance for further improvement of indoor thermal environment and energy-saving renovation for buildings.

When a radiant floor heating system operates intermittently, the zone air temperature varies at different stages of heat storage of the radiant floor. Some literature suggests that the exponential variation of the zone air temperature can be expressed as a pattern of heat transfer over time for the third-boundary conditions. The following assumptions were made to explain the specific application for the third-boundary conditions: (1) The exterior wall boundary is characterized by the average ambient air temperature. (2) The enclosure surface has a constant heat transfer coefficient and the third boundary condition is used to treat the inner enclosure surface (3) The one-dimensional heat transfer of the enclosures is homogeneous and constant.

The heat conduction equation of the interior partition is described as follows.

$$\frac{\partial t(x,\tau)}{\partial \tau} = a \frac{\partial^2 t(x,\tau)}{\partial x^2}, 0 < x \langle l, \tau \rangle 0 \qquad \text{Eq.1}$$

Where a refers to the thermal diffusion coefficient of interior partitions, m^2/s, l is half the thickness of the interior envelope, m. An initial condition is expressed as.

$$\tau = 0, t_0(x) = t_a, 0 < x < l \qquad \text{Eq.2}$$

where t_a refers to the initial zone air temperature. Boundary conditions are expressed as.

$$x = 0, \frac{\partial t(x,\tau)}{\partial \tau} = 0, \tau > 0 \qquad \text{Eq.3}$$

$$x = l, \lambda \frac{\partial t(x,\tau)}{\partial \tau} + a_a t(x,\tau) = a_a t_b(\tau), \tau > 0 \qquad \text{Eq.4}$$

Where λ refers to the thermal conductivity coefficient of interior partitions, $W/m \cdot K$, a_a refers to the convective heat transfer coefficient of interior partitions, $W/m^2 \cdot K$. $t_b(\tau)$ represents the zone air temperature.

Appling Duhamel's theorem to establish an auxiliary equation.

$$t(x,\tau) = f(x) + \int_{t=0}^{\tau} \frac{\partial}{\partial \tau} \emptyset(x, \tau - t, t) dt \qquad \text{Eq.5}$$

According to

$$\phi(x, \tau - t, t)|_{t=\tau} = \phi(x, 0, t) = f(x) \qquad \text{Eq.6}$$

By replacing the constant zone air temperature t_b with $t_b(\tau)$, the following equation can be obtained.

$$H_1 \qquad \text{Eq.7}$$

$$l_1 t_u \qquad \text{Eq.8}$$

β_m is a set of eigenvalues for the following characteristic equations:

$$tan\beta l = \frac{a_a}{\lambda \beta} \qquad \text{Eq.9}$$

And then the solution of the auxiliary equation can be obtained by integral transformation.

$$t(x,\tau) = t_a - \frac{a}{l^2} \sum_{n=1}^{\infty} \frac{2\beta_n^2 \sin\beta_n}{\beta_n + \cos\beta_n \cdot \sin\beta_n} \cos(\beta_n \frac{x}{l}) \int_{t=0}^{\tau} (t_a - t_b(t)) e^{\frac{-\beta_n^2 a(\tau-t)}{l^2}} dt$$

Eq.10

The temperature distribution inside the interior envelope can be obtained using the above characteristic equation by the corresponding temperature variation $t_b(\tau)$ (exponential, linear, etc.) while the zone air temperature varies according to a certain pattern, from which internal surface temperature and the heat flux inside the interior envelope can be derived.

Attenuation and delay occur as the temperature wave propagates from one side of the wall to the other due to the thermal inertia of the internal partition. The heat flux on the heated side of the inner wall is the effective heat dissipation for heating the zone air temperature, while the heat flux on the other side, i.e., close to the adjacent unheated room, is the ineffective heat dissipation, and the difference between the two is the heat stored in the inner partition at the current moment.

To clarify and better represent the ratio of the heat stored in the inner partition to the effective heat emitted into the heated room and the ratio of the accumulated heat of the inner partition to the total heat over time, the heat storage ratio φ_τ and the cumulative heat storage ratio $\emptyset$ of the interior partition is defined.

$$\varphi_\tau = \frac{q_{c\tau} - q_{n\tau}}{q_c \tau} \times 100\% \qquad \text{Eq.11}$$

$$\emptyset = \frac{\int_0^\tau (q_c - q_n)d\tau}{\int_0^\tau q_c d\tau} \times 100\% \qquad \text{Eq.12}$$

where φ_τ is the ratio of the heat storage flux of interior partitions to the total heat flux, $\emptyset$ is the cumulative heat storage ratio, $q_{c\tau}$ refers to the heat flux of interior partitions on the heating side, W/m^2, $q_{n\tau}$ refers to the heat flux of interior partitions on the adjacent-room side, W/m^2.

3. Simulation model

In this study, ANSYS software is used for the computational fluid dynamics simulation, ICEM is used for modeling, Fluent is used for numerical calculations, and CFD-Post is used for post-processing. The research procedure of the dynamic heat transfer performance of interior partitions is illustrated in Figure 1.

To investigate the heat flux variation on both sides of the interior partition, the CFD model of the two rooms and the internal partition wall was developed as shown in Figure 2, where the room B is heated with the partition surface AB_1 and room A is not heated with the partition surface AB_2. The surface AB_1 and surface AB_2 are the internal and outside surfaces of the interior partitions, respectively. The study focuses on the heat transfer performance of the internal partition between two chambers, of which each layer of the interior partition is modeled as a solid and the whole model contains a solid and a fluid region with a model grid number of 146949.

Considering the time-dependent fluid density under natural convection, the air density model uses the Boussinesq assumption, which is based on the principle that the buoyancy term in the momentum equation is used to calculate the density variation while the rest density terms in the equation are taken as constants. This kind of CFD model is suitable for applications with few fluid temperature changes, which can be applied for building models with little fluid temperature and density change in air conditioning systems.

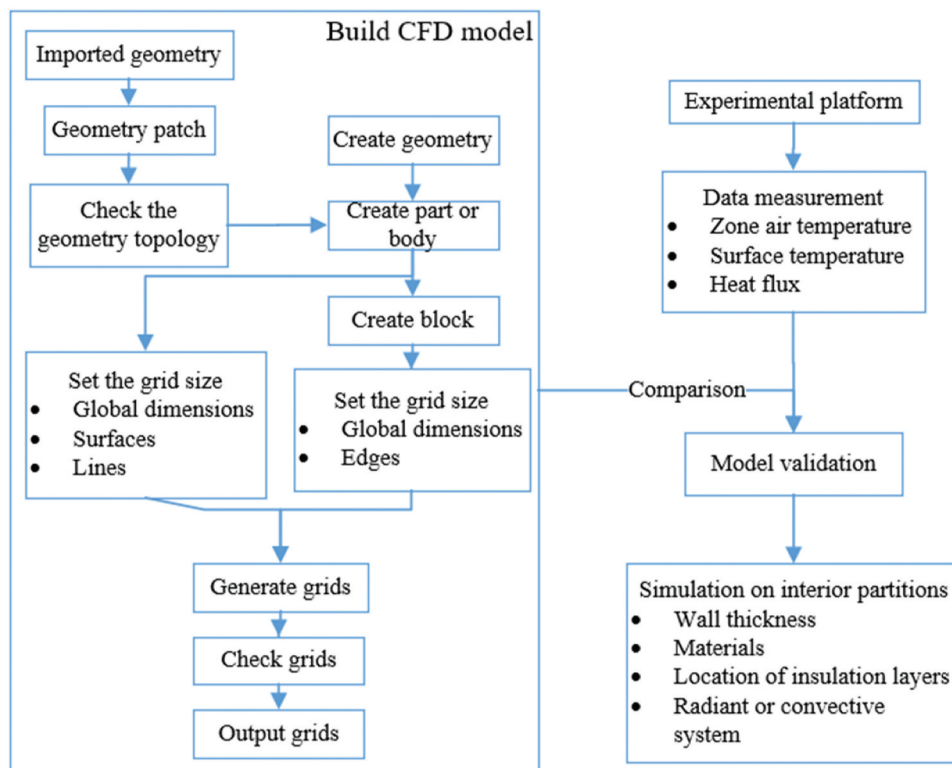The density in the buoyancy term can be expressed as.

Figure 1. The research procedure of the dynamic heat transfer performance of interior partitions.
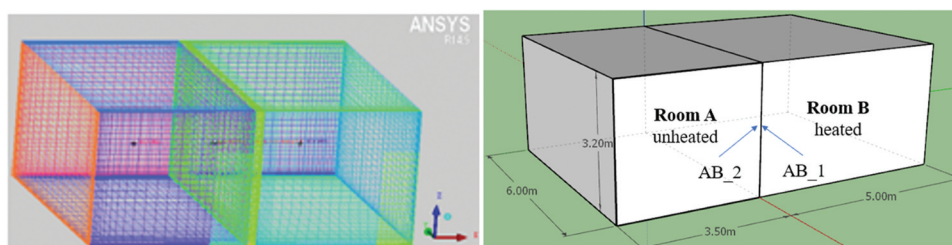
Figure 2. CFD model of the experimental rooms under radiant floor heating.

$$\rho = \rho_0[1 - \beta(T - T_0)] \qquad \text{Eq.13}$$

where T and T_0 refer to the transient and the lowest temperature in the fluid region and ρ_0 denotes the density of the reference fluid. β refers to the coefficient of thermal expansion.

In this study, the model grids are divided between 30 and 100, and the boundary layer is treated using the wall function method. The $k - \varepsilon$ Realizable model is used with the energy and radiation models turned on. The initial values in the simulation are determined from experimental data. The time step of the transient calculation is determined according to the empirical equation and its feasibility is verified by the simulation results. It is set to 5 seconds in this simulation after the calculation.

$$\Delta t = \frac{L}{(g\beta\Delta T \cdot L)^{1/2}} \qquad \text{Eq.14}$$

Where g refers to gravitational acceleration, m/s^2. β refers to the air expansion coefficient, ΔT is the temperature difference between the floor surface temperature and the average zone air temperature, $^{\circ}C$.

The average floor surface temperature of the experiment and simulation results is shown in Figure 3 with an average relative error of 0.05% between them, which is presented in Table 2. Ambient air temperature, floor surface temperature, other building envelope surface temperatures, and zone air temperature were measured by T-Type Thermocouple in the experiments. The supply and return water temperature, water flow rate, and heat supply of the radiant floor were obtained by calorimeter measurements. The heat flux of the floor surface, ceiling surface, and wall surface are obtained by heat flux sensor measurement. Details of the specific models, measurement ranges, and precision of the above measurement instruments used in the experiments are shown in Table 1.
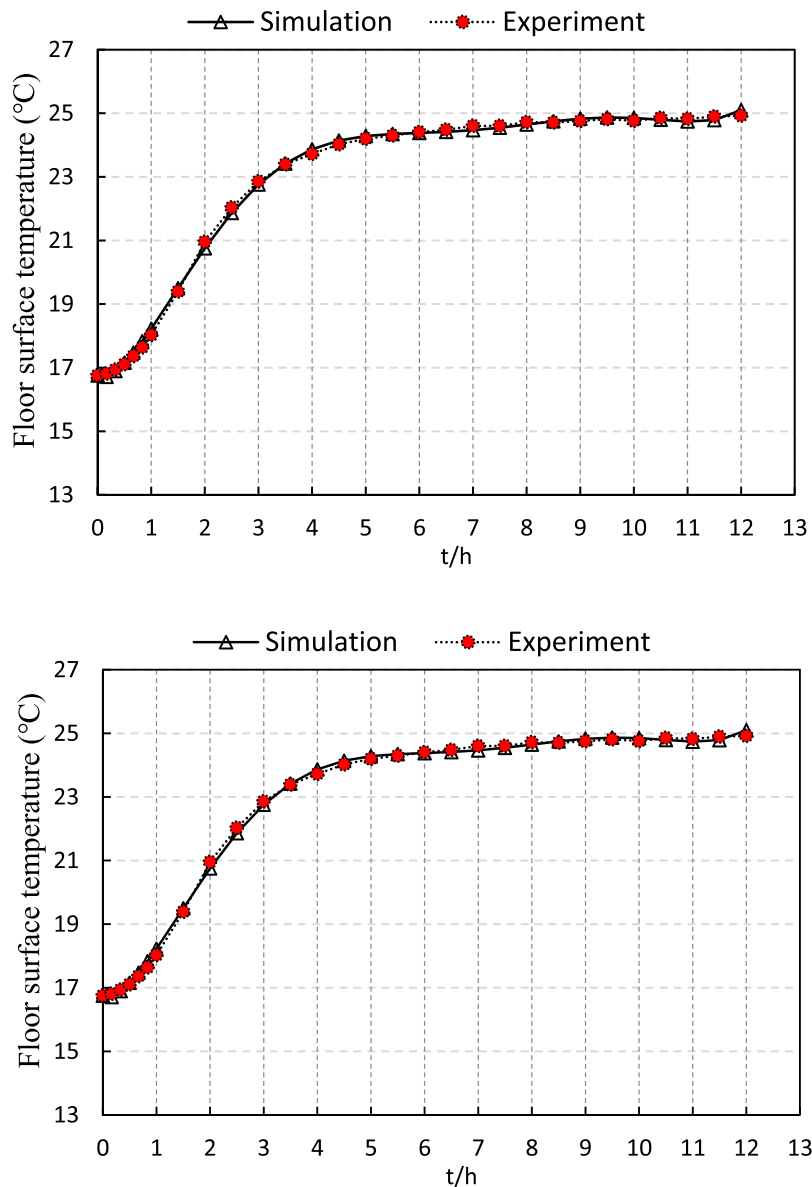

Figure 3. The average floor surface temperature of the experiment and simulation results.

Table 1. Details of the specific models, measurement ranges, and precision of the measurement instruments.

Instrument	Model	Measurement Range	Precision
Calorimeter	UH32-6.0	0°C~105°C	± 0.01°C
		0.02 m³/h~2.0 m³/h	± 0.001m³/h
		/	± 1 kW · h
T-Type Thermocouple	/	−40°C~+125°C	0.004 · |t| (After water-bath calibration)
Agilent Data Collector /	Agilent	34972A	−200°C~+350°C
HOBO temperature and humidity recorder	HOBO/	UX100-011 Temp:± 0.21°C	Temp:-20°C~70°C
Relative Humidity:1% ~95%	Relative	Humidity: ±3.5% (25% ~85%) ±2.5% (10%~90%)	
Thermal imager 1%	FLIR	T650sc	−40°C~150°C
Heat flux meter data loggers	DaqPRO 5300	Depending on the defined channel type	/
Heat flux sensor	HS-30	±200 kW/m²	3%

Table 2. Comparison of the simulation and the experimental results, including the zone air temperature, working-space temperature, and the surface temperatures of the building envelopes.

Location	Simulation (°C)	Measurement (°C)	Absolute error (°C)	Relative error (%)
z = 0.1 m	17.93	18.59	0.66	3.55%
z = 0.6 m	17.9	18.55	0.65	3.50%
z = 1.1 m	17.9	18.47	0.58	3.14%
z = 1.7 m	17.88	18.38	0.5	2.72%
z = 2.5 m	17.9	18.44	0.54	2.93%
Zone air temp	17.9	18.49	0.58	3.14%
AB_1	15.73	16.49	0.76	4.61%
Floor	22.31	22.30	0.01	0.05%
Ceiling	16.37	17.07	0.7	4.10%
Interior wall	15.32	16.03	0.71	4.43%
Exterior wall	14.39	14.33	0.06	0.42%

There are five temperature measurement points on the ceiling and the floor which are distributed in a "plum-shaped" pattern as shown in Figure 4a. The flow measurement points are arranged in the center of the ceiling and the floor surface as shown in Figure 4b. There are 9 temperature measurement points on the exterior wall and the interior partitions as shown in Figure 5a. The heat flux measurement points are arranged in the center of the wall surface, as shown in Figure 5b.

Twenty-five temperature measurement points are arranged in the working space as shown in Figure 6, and the temperature measurement points are arranged in the vertical direction at a height of 0.1 m, 0.6 m, 1.1 m, 1.7 m, and 2.5 m from the floor surface. Five measurement points at the same height are distributed in a "plum-shaped " pattern. Among them, 0.1 m is the height of the human ankle, 0.6 m is the height of the human knee and also the height of the person lying on the bed, 1.1 m is the height of the human head when sitting down, 1.7 m is the height of the human head when standing up.

Simulation and experimental results comparison including zone air temperature, internal surface temperature, average heat flux on the floor, and average heat flux on the ceiling is demonstrated in Figure 7. It can be seen that the simulated zone air temperature is consistent with the experimental results. The simulated surface temperatures of the interior partition have a good agreement with the experimental results. The two are almost the same in the phase of rapid warming while the experimental data is slightly higher than the simulated value during slower warming with a maximum relative error of 4.60%. It can be seen that the simulated heat fluxes on the floor surface and the ceiling surface is in good agreement with the experimental results as shown in Figure 7c, 7d, proving the great accuracy of the simulation model.

Comparison of the simulation and the experimental results, including the zone air temperature, working-space temperature, and the surface temperatures of the building envelopes are shown in Table 2. It can be seen that the relative error
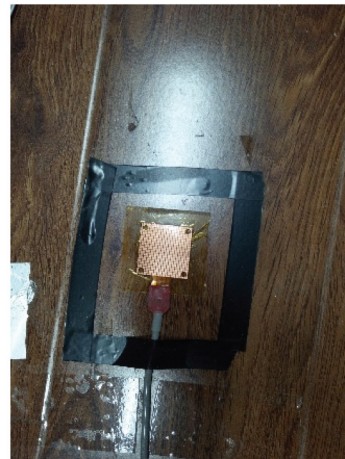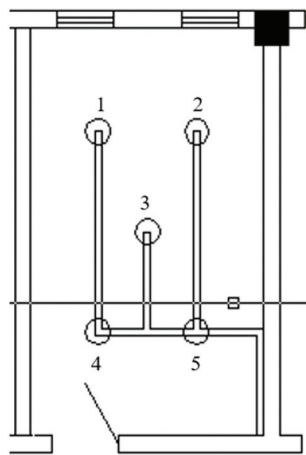

Figure 4. Schematic diagram of the temperature and heat flux measurement points distribution of the ceiling and the floor. (a) Temperature measurement (b) Heat flux measurement.

Figure 5. Schematic diagram of the temperature and heat flux measurement points distribution of the exterior wall and the interior partition.

Figure 6. Schematic diagram of the temperature measurement points in the working space.

between the simulation and experimental results under typical conditions is less than 5% which strongly illustrated the high reliability of the established CFD model.

5. Different configuration of interior partitions

The thermal properties of different configuration of internal partitions which significantly affect the dynamic heat transfer characteristics and energy consumption are investigated by numerical simulation after effective model validation. The main influencing factors include the material thermal resistance, the heat storage coefficient, thickness, and insulation layer location. Therefore, numerical simulations were carried out for seven typical configurations of interior partitions under radiant heating. Thermal property and geometry configuration parameters of seven kinds of interior partitions and other building enclosures are shown in Tables 3 and 4. The schematic diagram of seven kinds of interior partitions with different thicknesses, materials, and insulation layer locations is shown in Figure 8.

6. Results and discussion

6.1. Wall thickness

The average surface temperature and the average heat flux of the internal partition AB_1 and AB_2 are shown in

Figure 9. The results showed that the average surface temperature of the internal partitions did not change significantly for solid clay brick walls with thicknesses from 120 mm to 240 mm. The surface temperatures of 120 mm, 180 mm, and 240 mm walls were 15.67°C, 15.46°C, and 15.26°C, respectively, with a maximum difference of only about 0.41°C after 24 hours of continuous heating. These three curves almost coincided in the rising phase before the peak heat flux. The surface temperature of the adjacent unheated rooms gradually increased as the heat flux was obtained from the heated rooms. The temperature increases on the AB_2 surface of interior partitions with thicknesses of 120 mm, 180 mm, and 240 mm were 3.00°C, 2.53°C, and 2.12°C, respectively, after 24 hours of continuous operation. And the heat fluxes were 12.62 W/m², 10.83 W/m², and 9.34 W/m², respectively. Based on the variation trend of internal surface temperature and heat flux of the simulation results, the smaller the thickness of the interior partitions adjacent to the unheated chamber, the higher the internal surface temperature, and the lower the ineffective heat loss due to the non-heating of the adjacent chamber. Besides, the heat flux peaked after about 4.5 hours, which means that the interior partitions were experiencing a state of heat storage during the radiant floor was initially heated.

The heat storage ratio which reflected the ratio of real-time heat storage to the total heat flux supplied to the interior partition is shown in Figure 9e. It can be seen that the initial heat storage ratio stabilized at about 0.9 until the heat flux of the interior partition surface AB_1 peaked after about 4.5 hours, and then begin to decrease significantly. The cumulative heat storage rate of the internal partition is shown in Figure 9f, which reflected the ratio of the cumulative heat storage heat to the accumulated heat consumption of the interior partition. It can be seen that the cumulative heat storage ratios of all the three different thicknesses of the internal partitions were above 0.5 for 24 hours of radiant floor heating, which meant that the ratio of heat storage to the total heat flux of the internal partitions was greater than 50%, indicating that the heat storage proportion of the internal partitions was higher than that transferred to the adjacent unheated rooms. The unnecessary heat consumption transferred to the adjacent unheated room is 15.69 MJ, 12.93 MJ, 10.94 MJ in 24 hours for 120 mm, 180 mm, 220 mm solid clay brick walls according to the heat flux difference between surface AB_1 and AB_2. The 180 mm and 220 mm solid clay
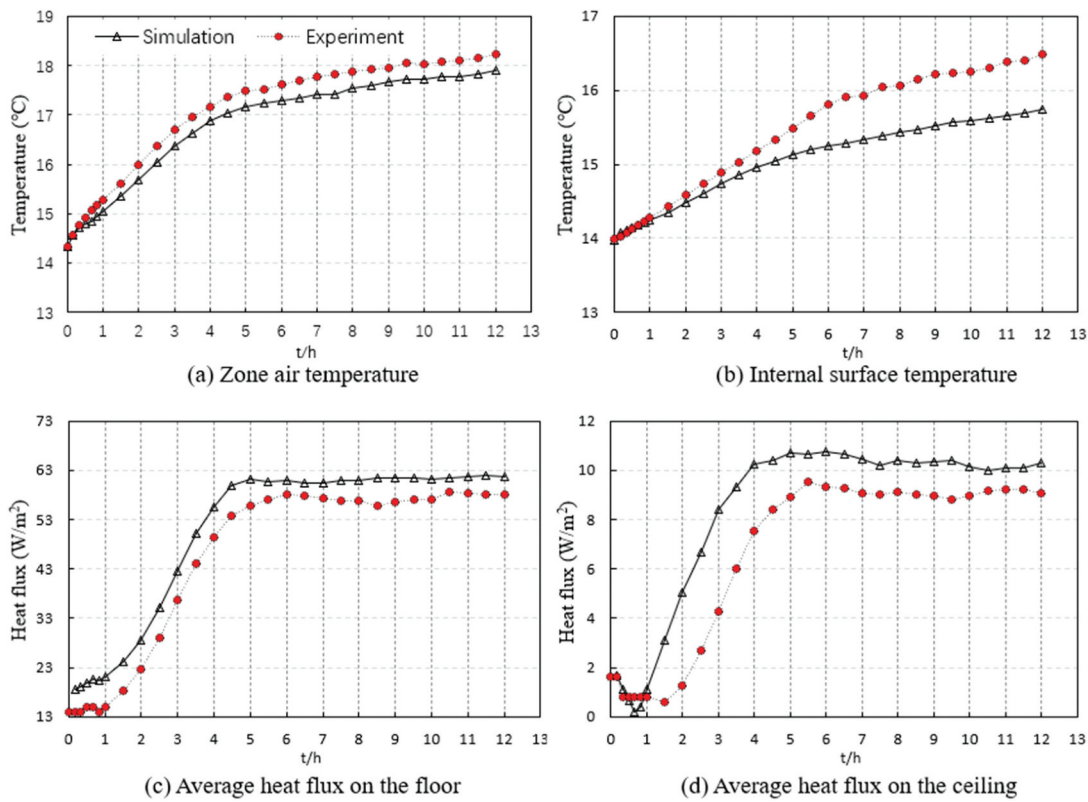
Figure 7. Simulation and experimental results comparison including (a) zone air temperature, (b) internal surface temperature, (c) average heat flux on the floor, and (d) average heat flux on the ceiling.

Table 3. Thermal property and geometry configuration parameters of seven kinds of interior partitions.

Number	Interior partitions	Thickness (mm)	Heat transfer coefficientW/(m² · K)	Thermal inertia index	Specific heat capacityJ/kg · K)	Thermal storage coefficientW/m² · K
1	120 Solid clay brick	160	2.379	1.861	879	11.37
2	180 Solid clay brick	220	2.024	2.574	879	11.37
3	240 Solid clay brick	280	1.761	3.288	879	11.37
4	180 Clay& Internal insulation	230	1.255	2.681	1791	9.7
5	180 Clay& External insulation	230	1.255	2.681	1791	9.7
6	180 Porous concrete	220	0.882	2.814	1791	9.7
7	180 Fly ash aerated concrete	220	0.882	3.549	1340	3.6

Table 4. Thermal property parameters of other building enclosures.

Envelope	Material	Thickness (mm)	Heat transfer coefficientW/(m² · K)	Thermal inertia index
Exterior wall	Solid clay brick	280	1.761	3.288
Window	Single-layer glass aluminum window	6	6.4	-
Floor	RC	130	3.054	-
Door	Cork	40	0.38	-
Other	interior walls Solid clay brick	220	2.024	2.574

brick walls can reduce energy consumption by 17.56% and 30.23% compared with the 120 mm solid clay brick.

6.2. Wall material

The dynamic heat transfer performance of three partition materials: solid clay brick, fly ash aerated concrete, and porous concrete are compared in this section. The thermal resistance of the fly ash aerated concrete walls and porous concrete walls are equal which is higher than that of the solid clay brick walls. The solid clay brick walls had the highest heat storage coefficient, followed by fly ash aerated concrete and porous concrete walls.

The surface temperature of the interior partitions increased rapidly first and then changed slowly during the continuous heating for 24 hours as shown in Figure 10. The heat flux of surface AB_1 peaked after 4 h ~ 4.5 h for experiencing a rapid increase, then followed by a slow decrease. The porous
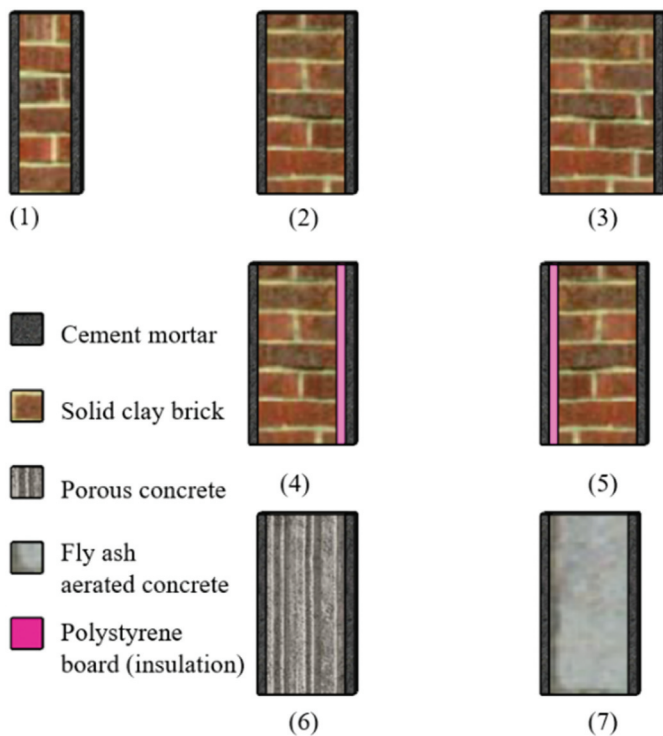
Figure 8. Schematic diagram of seven kinds of interior partitions with different thicknesses, materials, and insulation layer locations.

concrete partition had the highest stable average surface temperature (16.25°C), followed by fly ash aerated concrete partition (16.02°C) and solid clay brick (15.46°C) which was significantly lower than the former two. Solid clay brick bricks (24.96 W/m²) had the highest heat flux, followed by fly ash aerated concrete (21.09 W/m²) and porous concrete (19.35 W/m²). The temperature and heat flux of surface AB_2 of all three types of inner partitions showed a tendency to increase rapidly first and then slowly. The porous concrete had the highest surface AB_2 temperature (13.55°C), followed by solid clay brick (13.35°C) and fly ash aerated concrete (13.31°C) at the end of the heating phase. Porous concrete (11.56 W/m²) had the highest heat flux of surface AB_2, followed by fly ash aerated concrete (10.68 W/m²) and Solid clay brick (10.83 W/m²), which indicates that the heat flux through the porous concrete partitions to the adjacent unheated room was greatest, followed by solid clay brick and fly ash aerated concrete.

The heat storage ratio which reflected the ratio of real-time heat storage to the total heat flux supplied to the interior partition is shown in Figure 10e. It can be seen that the initial heat storage ratio stabilized at about 0.9 for about 1.5 hours, and then begin to decrease significantly. The heat storage ratio reduction of the solid clay brick wall was less than that of the other two partitions. Overall, the solid clay brick had the highest heat storage ratio, followed by fly ash aerated concrete and porous concrete. The cumulative heat storage ratio of the internal partition is shown in Figure 10f. It can be seen that only the porous concrete walls had a cumulative heat storage rate of less than 50% at the end, while the solid clay brick and fly ash aerated concrete walls had a cumulative heat storage

ratio of more than 50%, illustrating that the heat stored in the latter two partitions was greater than the heat transferred to the adjacent unheated rooms for 24 hours of continuous heating. The unnecessary heat consumption transferred to the adjacent unheated room was 12.93 MJ, 14.34 MJ, 15.97 MJ in 24 hours for solid clay brick, fly ash aerated concrete, and porous concrete partitions according to the heat flux difference between surface AB_1 and AB_2. The fly ash aerated concrete and solid clay brick partitions can reduce energy consumption by 10.18% and 19.02% compared with the porous concrete partitions.

6.3. Location of insulation layers

The surface temperature and the average heat flux on both sides of the interior partitions, the heat storage ratio, and the cumulative heat storage ratio of the interior partition with different insulation layer locations are shown in Figure 11. The surface AB_1 temperature variation trend of the interior partition with external insulation only slightly higher than that with no insulation layers, while the surface temperature of that with internal insulation layers was significantly higher than the former two. The surface AB_1 temperature was 15.24°C (uninsulated), 15.44°C (externally insulated), and 15.92°C (internally insulated), respectively, after 24 hours of continuous heating. The surface AB_1 heat flux of that with external insulation was slightly lower than that with no insulation layers and the heat flux of both interior partitions peaked after about 4.5–5 h, while the heat flux of that with internal insulation layers was significantly lower than that of the former two and the heat flux of that with internal insulation layers peaked after about 4 hours. The peak heat fluxes for the three interior partitions were 24.96 W/m² (uninsulated), 24.08 W/m² (externally insulated), and 17.45 W/m² (internally insulated).

It can be seen that the surface AB_2 temperature and heat flux of these interior partitions followed a different trend from the surface AB_1. The average surface temperature and heat flux of that with external and internal insulation were almost equal and significantly lower than with no insulation layers. The surface AB_2 temperatures of these interior partitions were 13.11°C (uninsulated), 12.50°C (internally insulated), and 12.54°C (externally insulated) at the end of 24 hours of heating, with average heat fluxes of 10.83 W/m² (uninsulated), 8.51 W/m² (internally insulated), 8.41 W/m² (externally insulated), respectively.

It can be seen that the externally insulated partition had the largest heat storage ratio, followed by the uninsulated and internally insulated partitions as shown in Figure 11(e). The heat storage ratio of the uninsulated, internally insulated and externally insulated solid clay brick partitions varies between 70% and 80% during the continuous heating of 24 hours as shown in Figure 11f. The externally insulated interior partitions had the highest heat storage ratio, followed by the uninsulated and internally insulated partitions. The unnecessary heat consumption transferred to the adjacent unheated room was 10.73 MJ, 8.62 MJ, 8.57 MJ in 24 hours for interior partitions with no insulation, internal insulation, and external insulation according to the heat flux difference between
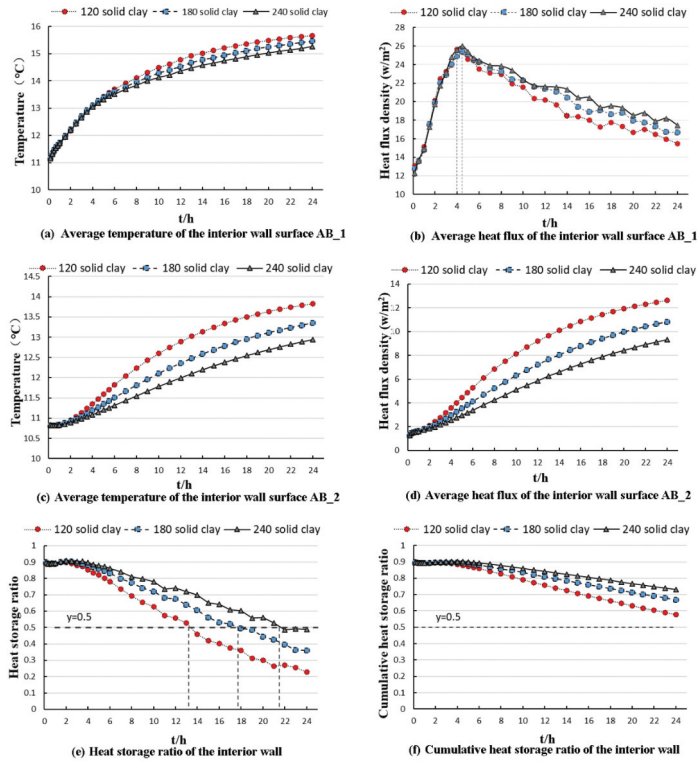
Figure 9. The surface temperature and the average heat flux on both sides of the interior partitions, the heat storage ratio, and the cumulative heat storage ratio of the interior partition with different thicknesses.

surface AB_1 and AB_2. The interior partitions with internal insulation and external insulation can reduce energy consumption by 19.63% and 20.12% compared with that with no insulation.

In general, the dynamic heat transfer performance of the interior partition with internal insulation was similar to that with external insulation owing to the relatively less unnecessary energy consumption transferred to the adjacent unheated rooms compared with that with no insulation. Comparison of the heat transfer characteristics and energy consumption of different wall thickness, materials, and insulation layer locations of interior partitions are summarized in Figure 12.

6.4. Radiant heating VS convective heating

The zone air temperature, the average surface temperature of the interior wall AB_1, and the vertical air distribution with radiant heating and convective heating system are shown in Figure 13. The zone air temperature under radiant floor heating condition (Case R) experienced two increasing stages and two decreasing stages with three peaks and troughs at 3.5 h, 10.5 h, and 11.5 h, respectively, which distributed in 17 ± 1°C. The zone air temperature under convective heating conditions (Case C) varied in the range of 19 ± 1°C. The radiant floor still supplied heat to the thermal zone even though the surface temperature drops due to the heat accumulation of the radiant floor. As a result, the surface temperature of AB_1 showed a slow rise and then a very slow downward trend during 210 min~570 min, dropping by 0.22°C in 6 h under the radiant heating condition (Case C). The surface temperature of AB_1 showed a slight decrease when the zone air temperature reached the setting values and the system switched to a lower heat supply under the convective heating condition (Case C). On the whole, the surface temperature of
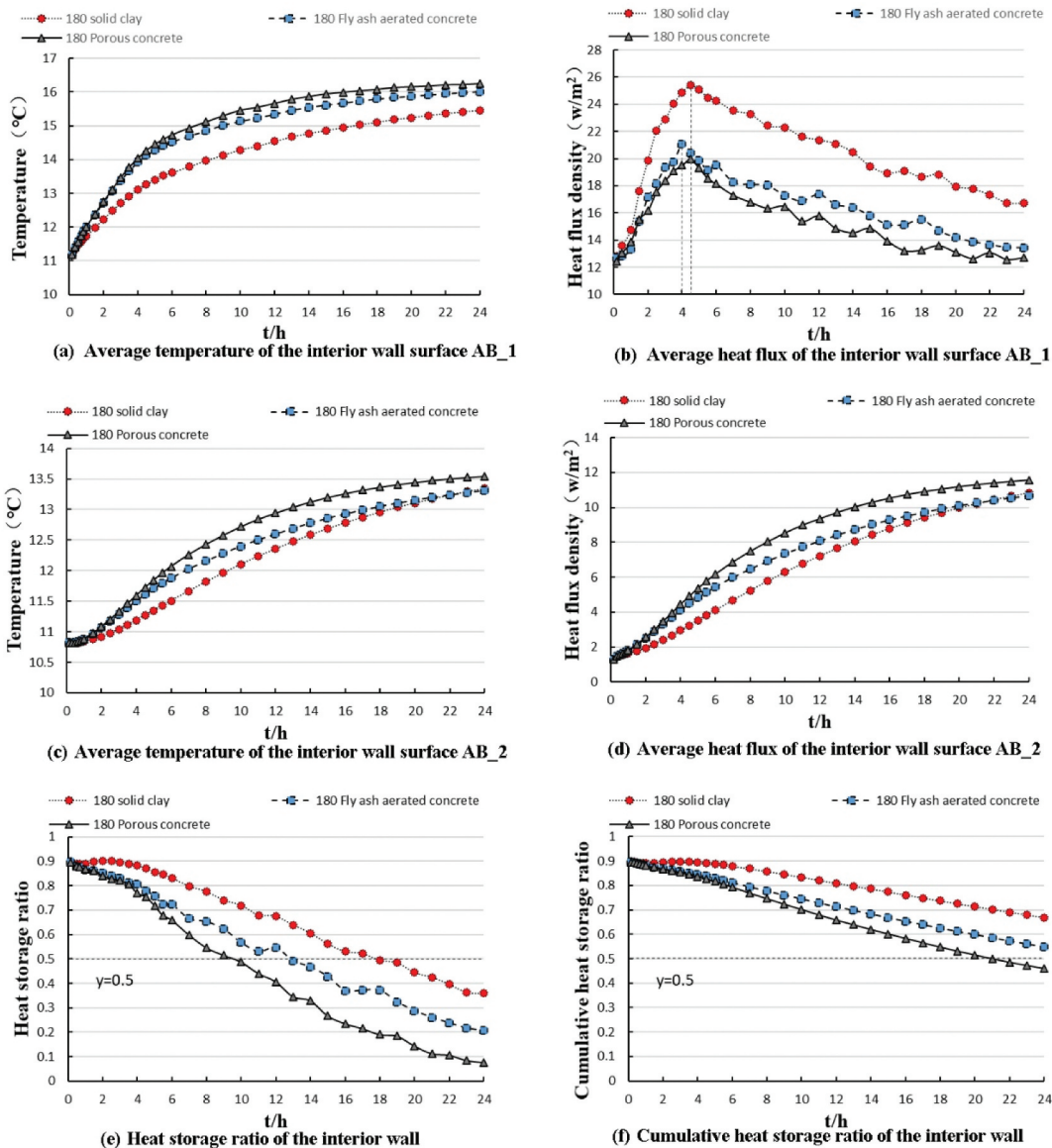
Figure 10. The surface temperature and the average heat flux on both sides of the interior partitions, the heat storage ratio, and the cumulative heat storage ratio of the interior partition with different materials.

AB_1 under convective heating was higher than that under radiant heating for almost all the time.

The reason for the higher surface temperature of the interior partitions under convection heating than radiant heating is derived from the inhomogeneity of the wall surface temperature under convection heating. Figure 13c and 13d shows the vertical air temperature distribution in the thermal zone under radiant and convective heating, respectively. The distribution of zone air temperature under the radiant heating was quite uniform at all times and the maximum vertical temperature difference in the working area was about 0.32°C, while the vertical temperature difference of zone air temperature under convective heating was relatively large and the lower zone of the heated room experienced a delay compared with increases with that of the upper zone. The vertical air temperature difference in the working area is 3.90°C, 6.38°C, 7.09°C, and 7.47°C at 0.5 h, 1.5 h, 6 h, 12 h, respectively.

The surface temperature distribution of the interior partition AB_1 at 400 min is shown in Figure 14. The temperature inhomogeneity of the AB_1 surface under convective heating was significantly higher than that under radiant heating. Moreover, the air supply temperature of the fan coil system (Case C) was required to be higher to achieve the same zone temperature in the working area while the air outlets were located in the upper space, resulting in a higher average surface temperature of the interior partition AB_1.

Heat consumption of interior partition and the total heat supply of the radiant and the convective system is shown in Table 5. The heat consumption of the interior partition was 2.504 MJ greater under convective heating (Case C) than that under radiant heating (Case R), which derived from 17.3% of the increased heat consumption transferred to the adjacent unheated room for 12 hours heating operation. The total heat consumption of the fan coil system (Case C) was at least 8.622 MJ less than that
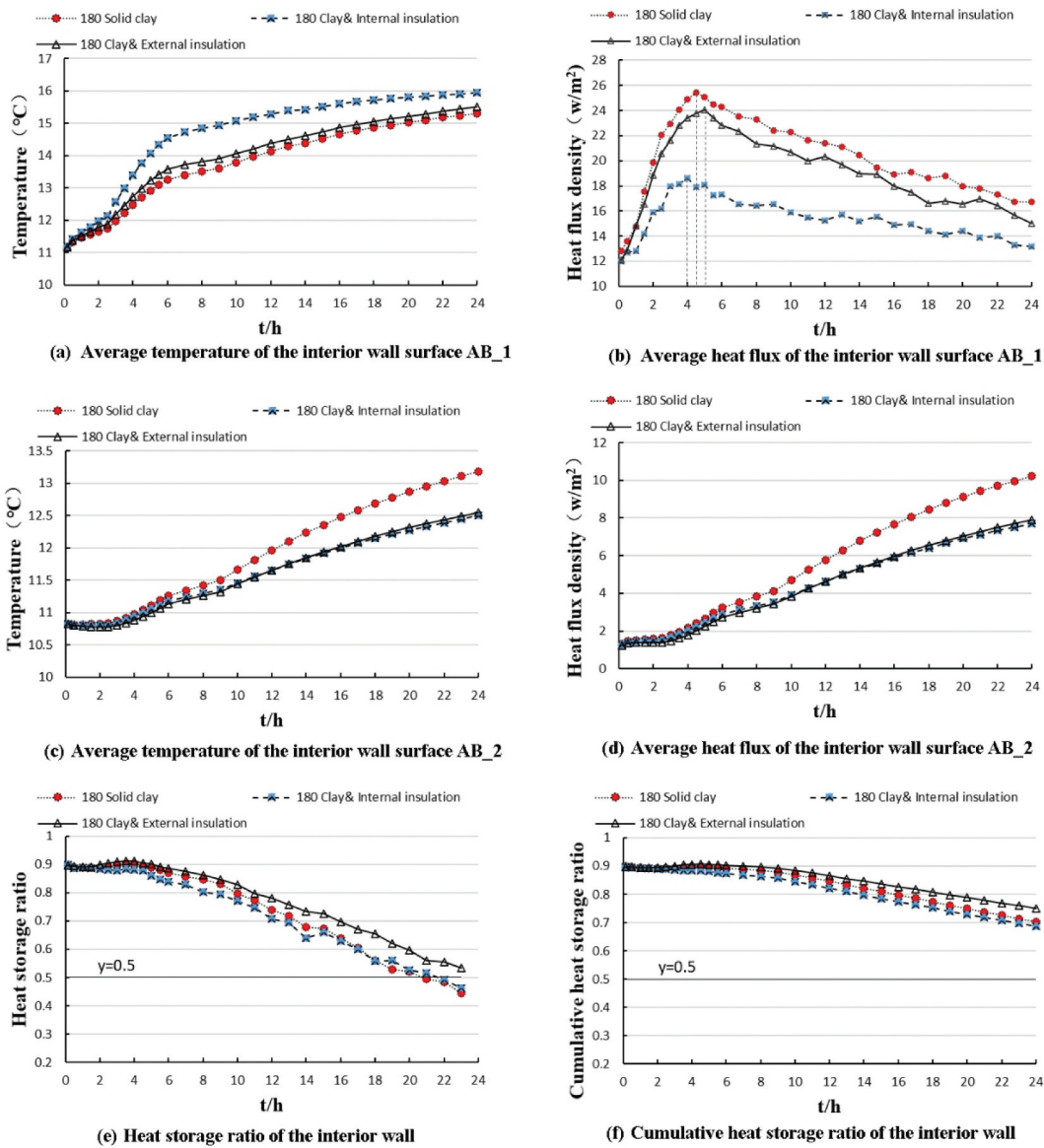
Figure 11. The surface temperature and the average heat flux on both sides of the interior partitions, the heat storage ratio, and the cumulative heat storage ratio of the interior partition with different insulation layer locations.

Figure 12. Comparison of the heat transfer characteristics and energy consumption of different wall thickness, materials, and insulation layer locations of interior partitions.
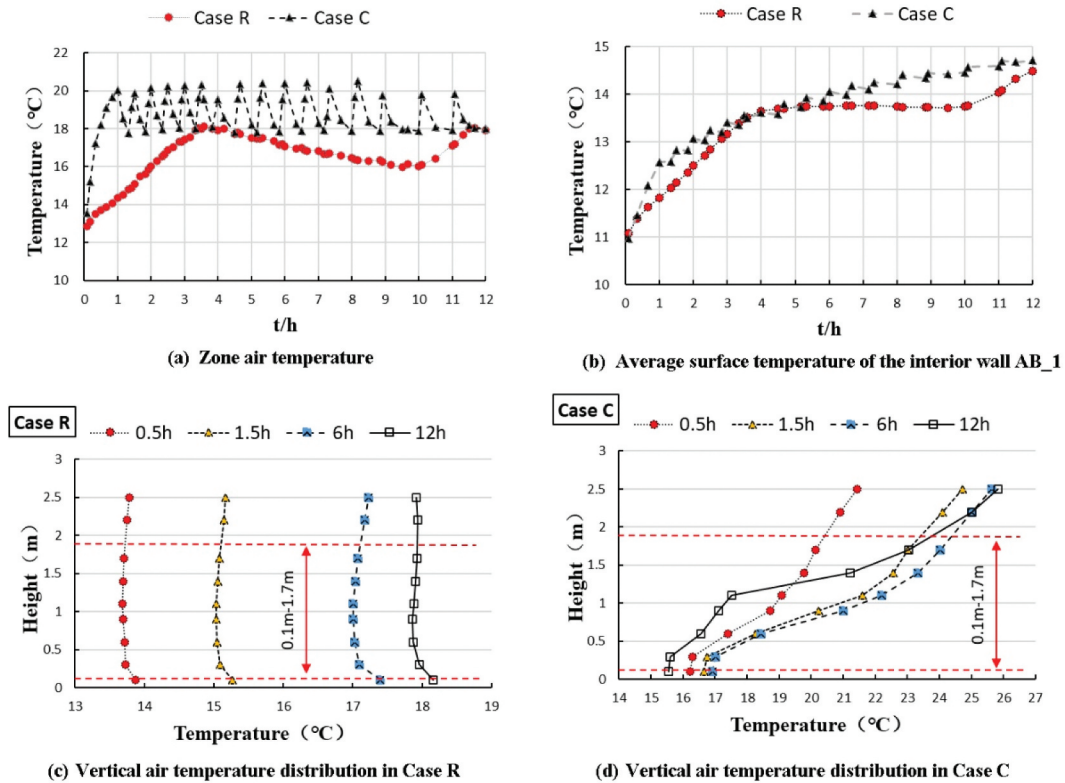
Figure 13. The zone air temperature, the average surface temperature of the interior wall AB_1, and the vertical air distribution with radiant heating and convective heating system.
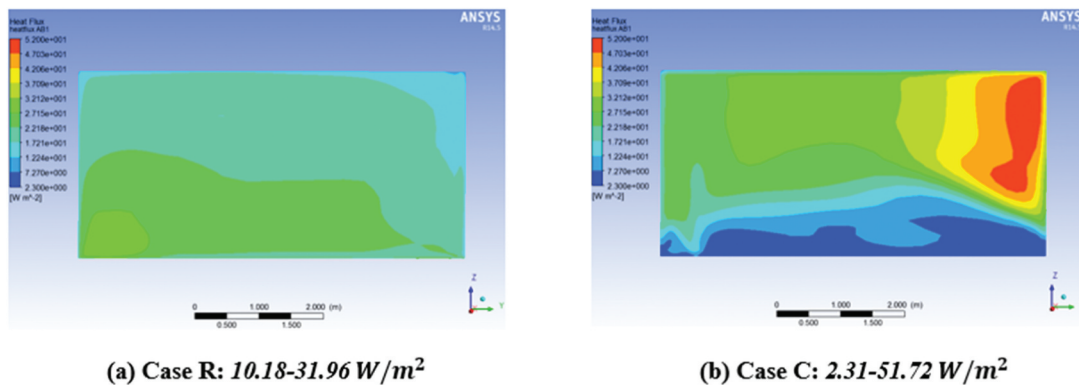

Figure 14. The surface temperature distribution of the interior partition AB_1 at the end of 12 hours of heating.

of the radiant floor system (Case R) with a different ratio of 11.7% due to the large inertia of the radiant floor.

7. Conclusion

In this study, the computational fluid dynamics model was built to evaluate the dynamic heat transfer characteristics of interior partitions in hot-summer and cold-winter zones. The experimental platform was built for the effective validation of the established CFD model, while the relative errors of the zone air temperature, the surface temperature, and the heat flux between the simulation and the experimental results were within 5%. Then, the seven typical configurations of interior

partitions with different thicknesses, materials, and insulation layer locations were evaluated after the accurate model validation finished.

The heat storage coefficient of internal partitions is an essential parameter for evaluating the dynamic heat transfer characteristics and energy consumption in winter in hot-summer and cold-winter zones in China. Although the relevant standards and regulations specify the detailed heat transfer coefficient of external envelopes (including ceiling, external walls, and windows), there are only a few requirements for the heat storage coefficient of internal partitions. Therefore, the standards are supposed to update the parameter limitations of building envelopes for energy-efficient operation facing the

Table 5. Heat consumption of interior partition and the total heat supply of the radiant and the convective system.

Heat capacity (MJ)	Case R	Case C	Relative ratio
Heat consumption of the interior partition	14.515	17.019	17.3%
The heat supply of the radiant floor	49.936	/	
The heat supply of the fan coil	/	70.120	
Heat consumption of the whole system	>82.433	73.811	−11.7%

Note: The heat transfer efficiency of the fan-coil system (convective system) was considered to be 95%.

prevailing trend of intermittent and distributed heating in this region.

The dynamic heat transfer performance of interior partitions is related to their thickness, material, location of insulation layers, and heating methods. The 180 mm and 220 mm solid clay brick walls can reduce energy consumption by 17.56% and 30.23% compared with the 120 mm solid clay brick. The fly ash aerated concrete and solid clay brick walls can reduce energy consumption by 10.18% and 19.02% compared with the porous concrete walls. The heat transfer performance of the interior partition wall with internal insulation is similar to that with external insulation owing to nearly 20% less unnecessary energy consumption transferred to the adjacent unheated rooms compared with that with no insulation. Therefore, the heat transfer performance of 220 mm solid clay brick with internal or external insulation is considered as the suggested option for interior partitions for intermittent heating among the commonly used partition configurations in hot-summer and cold-winter zones in China. The heat consumption of interior partitions under convective heating was 17.3% higher than under radiant heating for 12 hours heating, and the total heat consumption of the radiant heating system was 11.7% higher than that of the convective heating system due to the greater thermal inertia of the radiant floor. The cost-efficient evaluation of the initial investment of the building envelopes is supposed to be taken into consideration with the heating operation investment as well in further research.

Funding

References

Aguilar, F., J. P. Solano, and P. G. Vicente. 2014. Transient modeling of high-inertial thermal bridges in buildings using the equivalent thermal wall method. *Applied Thermal Engineering* 67 (1–2):370–77. doi:10.1016/j.applthermaleng.2014.03.058.

Al-Sanea, S. A., and M. F. Zedan. 2011. Improving thermal performance of building walls by optimizing insulation layer distribution and thickness for same thermal mass. *Applied Energy* 88 (9):3113–24. doi:10.1016/j.apenergy.2011.02.036.

Al-Sanea, S. A., M. F. Zedan, A. M. Al-Mujahid, Z. A. Al-Suhaibani. 2016. Optimum R-values of building walls under different climatic conditions in the kingdom of Saudi Arabia. *Applied Thermal Engineering* 96:92–106. doi:10.1016/j.applthermaleng.2015.11.072.

Al-Sanea, S. A., M. F. Zedan, and S. N. Al-Hussain. 2013. Effect of masonry material and surface absorptivity on critical thermal mass in insulated building walls. *Applied Energy* 102:1063–70. doi:10.1016/j.apenergy.2012.06.016.

Al-Tamimi, Ahmed S. Baghabra Al-Amoudi, Omar S. Al-Osta, Mohammed A. Ali, Mohammed R. Ahmad, Aftab. 2020. Effect of insulation materials and cavity layout on heat transfer of concrete masonry hollow blocks. *Construction and Building Materials* 254:119300. doi: 10.1016/j.conbuildmat.2020.119300.

Amiri Rad, E., and E. Fallahi. 2019. Optimizing the insulation thickness of external wall by a novel 3E (energy, environmental, economic) method. *Construction and Building Materials* 205:196–212. doi:10.1016/j.conbuildmat.2019.02.006.

Asdrubali, F., F. D'Alessandro, G. Baldinelli, F. Bianchi. 2014. Evaluating in situ thermal transmittance of green buildings masonries—A case study. *Case Studies in Construction Materials* 1:53–59. doi:10.1016/j.cscm.2014.04.004.

Axaopoulos, I., P. Axaopoulos, G. Panayiotou, S. Kalogirou, J. Gelegenis. 2015. Optimal economic thickness of various insulation materials for different orientations of external walls considering the wind characteristics. *Energy* 90:939–52. doi:10.1016/j.energy.2015.07.125.

Azmi, N. A., and S. H. Ibrahim. 2020. A comprehensive review on thermal performance and envelope thermal design of mosque buildings. *Building and Environment* 185:107305. doi:10.1016/j.buildenv.2020.107305.

Barrau, J., M. Ibañez, and F. Badia. 2014. Impact of the optimization criteria on the determination of the insulation thickness. *Energy and Buildings* 76:459–69. doi:10.1016/j.enbuild.2014.03.017.

Başoğul, Y., C. Demircan, and A. Keçebaş. 2016. Determination of optimum insulation thickness for environmental impact reduction of pipe insulation. *Applied Thermal Engineering* 101:121–30. doi:10.1016/j.applthermaleng.2016.03.010.

Bayoumi, M. 2017. Impacts of window opening grade on improving the energy efficiency of a façade in hot climates. *Building and Environment* 119:31–43. doi:10.1016/j.buildenv.2017.04.008.

Bond, D. E. M., W. W. Clark, and M. Kimber. 2013. Configuring wall layers for improved insulation performance. *Applied Energy* 112:235–45. doi:10.1016/j.apenergy.2013.06.024.

Chan, A. L. S. 2012. Effect of adjacent shading on the thermal performance of residential buildings in a subtropical region. *Applied Energy* 92:516–22. doi:10.1016/j.apenergy.2011.11.063.

Chang, S., D. Castro-Lacouture, and Y. Yamagata. 2020. Decision support for retrofitting building envelopes using multi-objective optimization under uncertainties. *Journal of Building Engineering* 32:101413. doi:10.1016/j.jobe.2020.101413.

Chorowski, M., Z. Rogala, and P. Pyrka. 2016. System options for cooling of buildings making use of district heating heat. *International Journal of Refrigeration* 70:183–95. doi:10.1016/j.ijrefrig.2016.06.018.

Cvetković, D., and M. Bojić. 2014. Optimization of thermal insulation of a house heated by using radiant panels. *Energy and Buildings* 85:329–36. doi:10.1016/j.enbuild.2014.09.043.

Daouas, N. 2011. A study on optimum insulation thickness in walls and energy savings in Tunisian buildings based on analytical calculation of cooling and heating transmission loads. *Applied Energy* 88 (1):156–64. doi:10.1016/j.apenergy.2010.07.030.

Hee, W. J., M. A. Alghoul, B. Bakhtyar, O. Elayeb, M. A. Shameri, M. S. Alrubaih, K. Sopian. 2015. The role of window glazing on daylighting and energy saving in buildings. *Renewable and Sustainable Energy Reviews* 42:323–43. doi:10.1016/j.rser.2014.09.020.

Hu, B., R. Z. Wang, B. Xiao, L. He, W. Zhang, S. Zhang. 2019. Performance evaluation of different heating terminals used in air source heat pump system. *International Journal of Refrigeration* 98:274–82. doi:10.1016/j.ijrefrig.2018.10.014.

Huang, H., Y. Zhou, R. Huang, H. Wu, Y. Sun, G. Huang, T. Xu. 2020. Optimum insulation thicknesses and energy conservation of building thermal insulation materials in Chinese zone of humid subtropical climate. *Sustainable Cities and Society* 52:101840. doi:10.1016/j.scs.2019.101840.

Idris, Y. M., and M. Mae. 2017. Anti-insulation mitigation by altering the envelope layers' configuration. *Energy and Buildings* 141:186–204. doi:10.1016/j.enbuild.2017.02.025.

Ihara, T., A. Gustavsen, and B. P. Jelle. 2015. Effect of facade components on energy efficiency in office buildings. *Applied Energy* 158:422–32. doi:10.1016/j.apenergy.2015.08.074.

Jie, P., et al.. 2019. Optimizing the insulation thickness of walls of existing buildings with CHP-based district heating systems. *Energy* 189: 116262. doi:10.1016/j.energy.2019.116262.

Kumar, D., M. Alam, P. X. W. Zou, J. G. Sanjayan, R. A. Memon. 2020. Comparative analysis of building insulation material properties and performance. *Renewable and Sustainable Energy Reviews* 131:110038. doi:10.1016/j.rser.2020.110038.

La Rosa, A. D., A. Recca, A. Gagliano, J. Summerscales, A. Latteri, G. Cozzo, G. Cicala. 2014. Environmental impacts and thermal insulation performance of innovative composite solutions for building applications. *Construction and Building Materials* 55:406–14. doi:10.1016/j.conbuildmat.2014.01.054.

Li, Z., D. Zhang, and C. Li. 2021. Experimental evaluation of indoor thermal environment with modularity radiant heating in low energy buildings. *International Journal of Refrigeration* 123:159–68. doi:10.1016/j.ijrefrig.2020.11.018.

Mathur, U., and R. Damle. 2021. Impact of air infiltration rate on the thermal transmittance value of building envelope. *Journal of Building Engineering* 40:102302. doi:10.1016/j.jobe.2021.102302.

Natephra, W., N. Yabuki, and T. Fukuda. 2018. Optimizing the evaluation of building envelope design for thermal performance using a BIM-based overall thermal transfer value calculation. *Building and Environment* 136:128–45. doi:10.1016/j.buildenv.2018.03.032.

Özel, G., E. Açıkkalp, B. Görgün, H. Yamık, N. Caner. 2015. Optimum insulation thickness determination using the environmental and life cycle cost analyses based entransy approach. *Sustainable Energy Technologies and Assessments* 11:87–91. doi:10.1016/j.seta.2015.06.004.

Ozel, M. 2012. The influence of exterior surface solar absorptivity on thermal characteristics. *Renewable Energy* 39 (1):347–55. doi:10.1016/j.renene.2011.08.039.

Ozel, M. 2013. Determination of optimum insulation thickness based on cooling transmission load for building walls in a hot climate. *Energy Conversion and Management* 66:106–14. doi:10.1016/j.enconman.2012.10.002.

Ozel, M., and K. Pihtili. 2007. Optimum location and distribution of insulation layers on building walls with various orientations. *Building and Environment* 42 (8):3051–59. doi:10.1016/j.buildenv.2006.07.025.

Rosti, B., A. Omidvar, and N. Monghasemi. 2020. Optimal insulation thickness of common classic and modern exterior walls in different climate zones of Iran. *Journal of Building Engineering* 27:100954. doi:10.1016/j.jobe.2019.100954.

Sheng, W., B. Wen,L, and L. Zhang. 2021. Zhang, Envelope performance of residential building in cool, warm and hot climatic zones: Results from self-designed in-situ monitoring campaigns. *Energy and Buildings* 232:110655. doi:10.1016/j.enbuild.2020.110655.

Wang, Z., Y. Qiao, Y. Liu, J. Bao, Q. Gao, J. Chen, H. Yao, L. Yang. 2021. Thermal storage performance of building envelopes for nearly-zero energy buildings during cooling season in Western China: An experimental study. *Building and Environment* 194:107709. doi:10.1016/j.buildenv.2021.107709.

Xu, L., L. Dai, L. Yin, X. Sun, W. Xu, R. Yang, X. Wang, Y. Zhang. 2020. Research on the climate response of variable thermo-physical property building envelopes: A literature review. *Energy and Buildings* 226:110398. doi:10.1016/j.enbuild.2020.110398.

Yamamoto, T., A. Ozaki, S. Kaoru, K. Taniguchi. 2021. Analysis method based on coupled heat transfer and CFD simulations for buildings with thermally complex building envelopes. *Building and Environment* 191:107521. doi:10.1016/j.buildenv.2020.107521.

Zhang, X., and X. Zhang. 2020. A subproject-based quota approach for life cycle carbon assessment at the building design and construction stage in China. *Building and Environment* 185:107258. doi:10.1016/j.buildenv.2020.107258.

Ziapour, B. M., M. Rahimi, and M. Y. Gendeshmin. 2020. Thermoeconomic analysis for determining optimal insulation thickness for new composite prefabricated wall block as an external wall member in buildings. *Journal of Building Engineering* 31:101354. doi:10.1016/j.jobe.2020.101354.